Gradient light video projection-based stereolithography for continuous production of solid objects

Ketki M. Lichade, Erina Baynojir Joyee, Yayue Pan *

Department of Mechanical and Industrial Engineering, University of Illinois at Chicago, Chicago, 60607, USA

ARTICLE INFO

ABSTRACT

The Video Projection-based Stereolithography (VP-SL) is a fast, low-cost, and high-resolution additive manufacturing (AM) process. However, critical issues, including manufacturing defects such as holes in the solid geometry and manufacturing constraints such as limited size, have been reported. To successfully print a part, the light exposure intensity needs to be carefully controlled. In this paper, a gradient light video projection-based stereolithography (GLVP-SL) process with continuous resin flow is presented. The newly developed AM process enables the continuous fabrication of three-dimensional (3D) solid objects with controlled exposure energy. For each layer, instead of a single image, three mask images are designed with unique grayscale distributions. The effect of grayscale distribution on printing process characteristics including the curing speed and resin flow, is investigated. An optimization model to identify the optimum grayscale distribution pattern for the desired size and density of the solid structure is developed. For comparison, various solid objects were printed with the conventional VP-SL process and our proposed GLVP-SL process. The porosity and surface roughness of the printed parts were characterized. Experimental results validated that the GLVP-SL process can print void-free 3D solid objects with a good surface quality.

1. Introduction

Mask Image Projection-based Stereolithography (MIP-SL) is an additive manufacturing (AM) process that uses light projection device (for example, digital micromirror device and light crystal display), to manage the exposure energy on the liquid photoresin [1] and to build a 3D object through selective photopolymerization. It has been implemented in a wide range of applications, including tissue engineering [2], biomedicine [3,4], and microelectronic devices [5]. MIP-SL can be categorized into two types: layer-by-layer based printing [6,7] and continuous (i.e., layer-less) printing, also known as Video Projection-based Stereolithography (VP-SL) [8–10]. In the layer-by-layer process, a three-dimensional (3D) CAD model is sliced into a set of two-dimensional (2D) images and projected onto the resin surface using a light projection device to form a solid layer. The process is repeated to create a three-dimensional solid structure. However, the stair-stepping effect limits the surface quality of the parts fabricated layer by layer. In addition, because of the layer projection and separate liquid recoating, the printing speed is limited to a few millimeters per hour [8]. In contrast, VP-SL is a process in which the curing part is drawn out of the resin tank continuously with simultaneous curing and pulling. Recently, VP-SL has gained a lot of attention due to the layerless fabrication of complex 3D structures and orders of magnitude faster printing speed compared to the layer-by-layer process [10].

Considering these advantage, various VP-SL based technologies have been developed, mainly using two approaches: oxygen inhibition window [11–14] and continuous liquid flow [15,16]. For example, Tumbleston et al. developed the Continuous Liquid Interface Production (CLIP) process that enables high-speed (hundreds of millimeters per hour) production of microscopic as well as macroscopic parts [11]. This was achieved by replacing the conventional tank with a transparent oxygen-permeable film (Teflon AF 2400). In a previous work, our group developed a simple yet highly effective island-window design for the continuous 3D printing by using the VP-SL process. The proposed constrained window design had a highly oxygen-permeable PDMS membrane coated onto a lasermachined acrylic vat frame, which allows the formation of an effective liquid interface (>200 μm oxygen inhibition layer) to enable the continuous printing process [13,14]. Moreover, Li et al. demonstrated a Mask Video Projection-based Stereolithography process (MVP-SL), in which a continuous side motion along X-axis was

---

* Corresponding author.
  E-mail address: yayuepan@uic.edu (Y. Pan).

integrated using an additional linear stage [15]. Walker et al. used a pumped, nonreactive fluorinated oil to act as the dead layer that removes heat during polymerization, which allows for both speedup and scale-up of the printing process [16].

Although these techniques have enabled the continuous fabrication of complex structures, significant challenges still exist in the production of solid geometry with a large cross-section area due to the difficulty of balancing continuous liquid curing and liquid flow processes. For example, to maintain a printing speed and avoid coating failure, the CLIP process can only fabricate hollow geometries with a relatively smaller cross-section area. The shear force due to the viscous drag and unstable oscillation of liquid resin caused by the moving stage in the MVP-SL process affects the printing quality, including holes in printed parts. Moreover, increasing the thickness of the oxygen-permeable window can affect the printing performance, and adding hardware in the system can make it bulky and complicated.

A commonly documented approach for improving printing quality and eliminating manufacturing defects is the use of gradient (i.e., non-uniform) light projection. In this approach, instead of black-white binary images, gray-scale images are projected to the liquid resin surface to selectively cure liquid resin to form a solid layer. Extensive research has been conducted to study the effect of gradient light on curing properties of the liquid resin and overall printing performance in the layer-by-layer MIP-SL [1,17–23]. Many researchers have implemented the grayscale mask image projection approach in their research; for example, Ma et al. [17] proposed a multiple patterning method to improve fabrication accuracy. Instead of using one mask image, this method involves the projection of multiple mask images with varied grayscale designs to fabricate a 3D structure. Zhou et al. [1,18,19] reported new methods to achieve better accuracy and part quality by setting optimum grayscale values of the individual pixel of the projection image based on the critical exposure energy. In addition, Park et al. [20] developed another technique for improving the surface quality of the fabricated part by controlling the light intensity distribution using 2D grayscale mask images. From the literature review, it was found that in the layer-by-layer MIP-SL process, the gradient light can improve the overall printing quality of objects with large solid cross-section areas. In addition, it is an easy-to-implement, low cost, and time-efficient method.

Despite the advantages and common use of the grayscale image in the layer-by-layer MIP-SL processes, very few studies investigated its use in the VP-SL process. Recently, Wang et al. used the grayscale display method in the VP-SL process to improve the printing resolution and area of the structures by modifying mask images into grayscale [24]. Quality of the continuously printed parts showed significant progress, especially for mesh and hexahedron frame construct. To the author's best knowledge, no study has been reported about integrating grayscale images into the VP-SL process for the fabrication of objects with large solid cross-sections. A major challenge in continuously printing solid objects using varied grayscale distribution is the absence of a systematic study on how to establish the relationship among grayscale values, exposure energy, curing speed, and resin flow. Optimization of the grayscale distribution is the key to achieving controlled exposure energy for selectively curing and accumulating material at the desired locations during the VP-SL process.

In this study, a novel AM process, named Gradient Light Video Projection-based Stereolithography (GLVP-SL) is proposed. In the conventional VP-SL method, a set of sliced layers are transformed into 2D binary images which are continuously projected like a video onto the resin surface. In comparison, in our GLVP-SL method, each sliced image is divided into three mask images with unique grayscale distribution patterns. By manipulating the grayscale values of the projection images, the total exposure energy of each unit liquid entering the projection area at a certain time can be controlled. With an objective of enabling solidification of each unit liquid at its target curing position (δ_t), first, the relationships between the exposure energy (E'), curing speed, and resin

flow were studied as a function of projection time and grayscale value. Then, the mask image planning algorithm was developed to predict the grayscale distribution for each mask image based on the target curing position. The resulting exposure energy E was measured and compared with the target exposure energy E'. Next, the sequence of grayscale mask images with optimized grayscale distribution was generated and applied to print various solid geometries. The porosity and surface roughness of printed models were characterized and compared to the conventional VP-SL printing. This method allows the minimization of printing errors in the solid objects, taking into account the total energy received in any spatial and temporal location during the GLVP-SL printing.

The rest of the article is organized as follows: Section 2 describes the experimental setup for the typical VP-SL process. Section 3 provides an overview of the GLVP-SL process, including the proposed grayscale distribution design and process planning workflow. Section 4 develops the optimization method to design the grayscale distribution for mask images based on the target curing position by studying the effect of grayscale values on the exposure energy, curing properties, and resin flow. To validate the feasibility of the proposed method, section 5 presents several test cases to compare the porosity, surface roughness, and printing capability of the VP-SL and GLVP-SL methods. Lastly, section 6 summarizes this study and its findings.

2. Experimental setup

In this study, a typical VP-SL setup was developed to investigate the proposed GLVP-SL process, as shown in Fig. 1. In the setup, a Digital Light Processing (DLP) Lightcrafter™ 4500 projection module from Texas Instruments (Dallas, Tx) was used for projecting a dynamic mask video using a digital micromirror device (DMD). A linear stage (Velmex Inc., USA) was used for continuously moving the platform along the Z-axis. A software was developed using the C++ program to control and synchronize the Z movement with the light projection.

To monitor the printing process in real time, a high-resolution load cell (FUTEK Advanced Sensor Technology Inc., USA) was also integrated into the system. A separate program was developed in Matlab to monitor any insignificant changes in the significant force. A resin tank with circular air-diffusion channels was made using 1.25 mm thick acrylic sheets. The air-diffusion channels on the acrylic plate were fabricated by laser micromachining (Universal Laser Systems, USA). The bottom surface of the resin tank was made of a 2 mm thick PDMS (Sylgard 184, Dow Corning) layer coated on a porous acrylic plate. The PDMS coating was made by mixing the base polymer and a curing agent with a 10:1 volume ratio [13]. Makerjuice Standard (MakerJuice Labs, USA) with a viscosity of 250 cP @ 20 °C was used as the liquid photopolymer in this study.

3. Design of gradient light video projection-based stereolithography

3.1. Overview of GLVP-SL

When a black-white binary mask image is projected during the VP-SL process, a unit liquid gets fully cured to solid when it receives the energy required for full polymerization. However, since the light energy to each unit liquid is identical while the traveling distance required for being cured at the target position varies among unit liquids, some resin may get solidified before reaching its target position while some may flow pass the target position, as illustrated in Fig. 2a. This can result in undesired rough layer boundary and porous interior structure.

This paper proposed a gradient light video projection approach to avoid such printing defects or failures. In our gradient light video projection approach, instead of one binary mask image for curing one sliced layer, three grayscale mask images with gradient light energy distributions are designed for one sliced layer and thus a gradient light video is generated for continuous polymerization. Let the exposure time for one
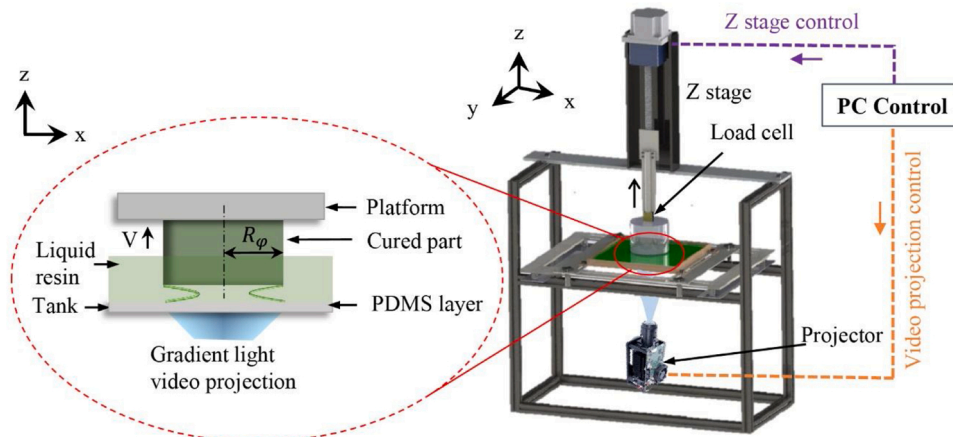
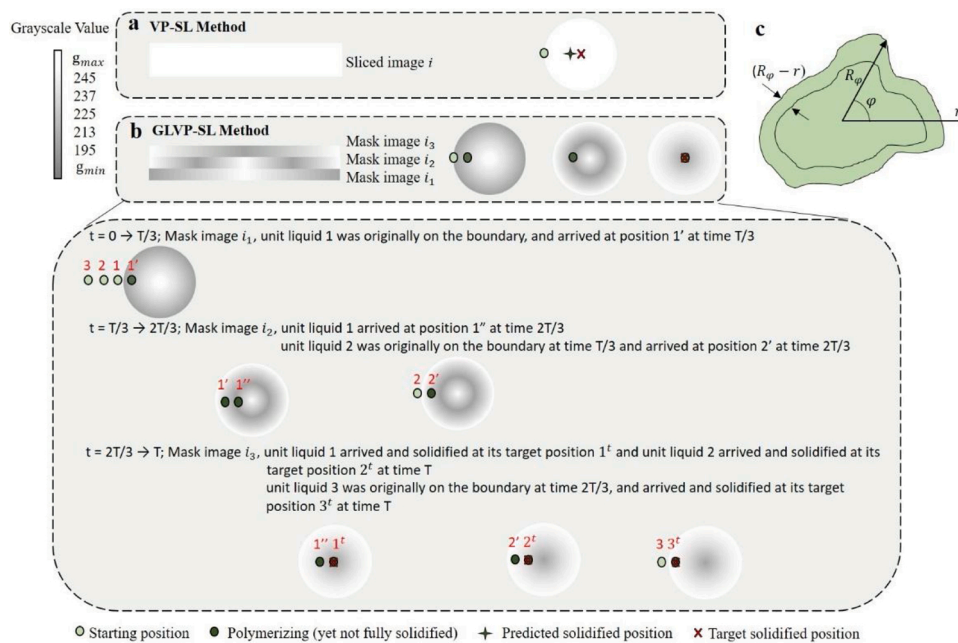**Fig. 1.** Illustration of the experimental setup for a typical VP-SL process.

Fig. 2. Grayscale distribution design and hypothetical mechanism for: (a) conventional VP-SL, (b) novel GLVP-SL process, and (c) irregular solid cross-section and the polar coordinate system.

sliced layer to be T. To increase the printing quality without increasing the printing time, each sliced layer generates three mask images with an identical projection time $T/3$. By manipulating the grayscale values of the three mask images i_1, i_2, and i_3, unit liquids entering the projection area at different timing, e.g., unit liquid 1, 2, and 3 in Fig. 2b, will receive light energy with different intensities and get fully solidified at their target positions (e.g., positions 1^t, 2^t, and 3^t for unit liquids 1, 2, and 3, respectively) instead of being solidified before or after flowing to their target positions. To achieve this goal, each mask image is designed with a step-wise modulation of grayscale values, as illustrated in Fig. 2b and modeled as follows:

$$g(\delta, t) = \begin{cases} -m\,\delta + g_{max}, & \text{for } 0 < t < \dfrac{T}{3} \ (\text{mask image 1}) \\[2mm] m \times |2\delta - 1| + g_{min}, & \text{for } \dfrac{T}{3} \le t < \dfrac{2T}{3} (\text{mask image 2}) \\[2mm] m\,\delta + g_{min}, & \text{for } \dfrac{2T}{3} \le t \le T \ (\text{mask image 3}) \end{cases} \quad (1)$$

where, m is the difference between g_{max} and g_{min}, and δ is the

dimensionless position measured as the ratio of the location of a unit liquid before solidifying $((R_\varphi - r))$ and the size of the mask image with respect to angle φ (R_φ), as shown in Fig. 2c.

In a general form, the grayscale value from mask images 1–3 is gradually increasing on layer boundary and gradually decreasing at the center between the ranges g_{min} (0–255) to g_{max} (255). The same design strategy is implemented for designing grayscale mask image frames for all layers and thereafter generating a gradient light video for the 3D object continuous printing.

3.2. Workflow of GLVP-SL

The video generation procedure for the proposed GLVP-SL process is illustrated in Fig. 3. First, a 3D CAD model is created and then sliced into 2D slices. The projection time per slice is decided based on the platform lifting speed and the slicing thickness. Each sliced image is then divided into three individual grayscale mask images, and the individual grayscale pattern is used to generate each. Finally, a video was generated by combining these grayscale mask images. During the video generation
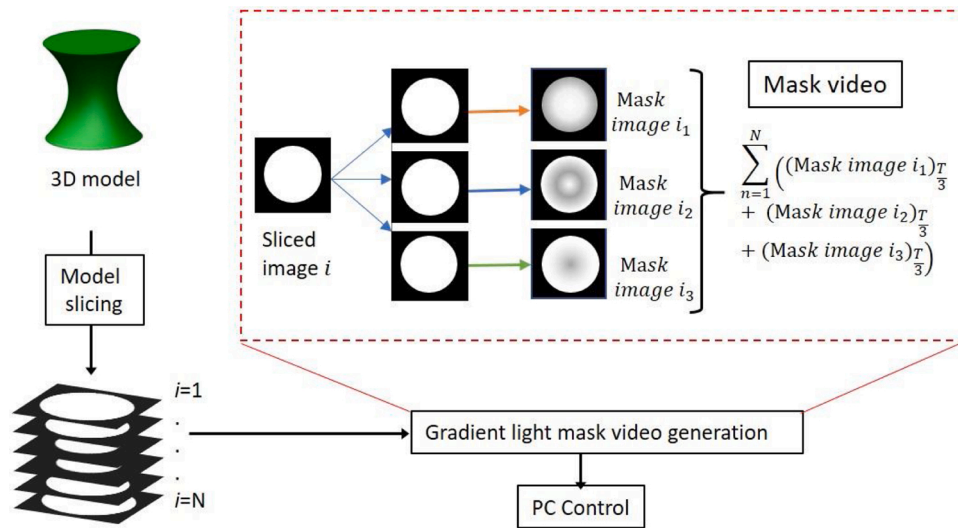
Fig. 3. Video generation procedure in the GLVP-SL process.

process, the projection time for each grayscale mask image is set as 1/3 of the projection time for one slice. Accordingly, the video projection time t_v will be:

$$t_v = \sum_{i=1}^{N} \left(\left(\text{Mask image } i_1\right)_{\frac{T}{3}} + \left(\text{Mask image } i_2\right)_{\frac{T}{3}} + \left(\text{Mask image } i_3\right)_{\frac{T}{3}} \right) \quad (2)$$

here, i is the number of sliced image and T is the projection time for one sliced image, and N is the number of sliced images.

A flowchart of the GLVP-SL process is shown in Fig. 4. To start with the printing process, first, the platform is brought to the initial position, and a base layer is printed to ensure that the newly cured part will stick to the platform. The video is then continuously projected by a DLP projector through the transparent bottom surface of the resin tank, onto the liquid resin surface. A part is continuously cured and drawn out of the resin tank simultaneously by the platform, which is continuously
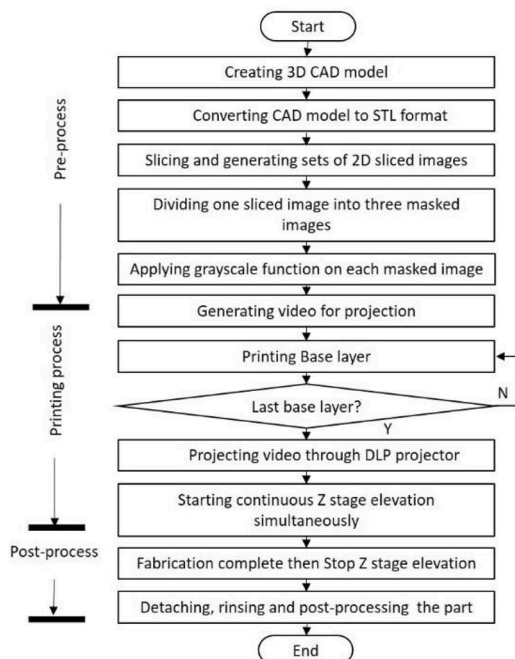
moving up along the Z-axis. When the video projection is ended, the part is completely printed. Then it can be removed from the platform for cleaning, post-processing, and application.

4. Process characterization and modeling of GLVP-SL

4.1. Effect of grayscale image on exposure energy

Recently, grayscale has been applied to control the intensity and exposure distribution in the stereolithography process. To determine the relationship between grayscale and exposure energy, a circular image of diameter 30 mm was projected onto the tank in the absence of resin. Grayscale varying from 50 to 255 was applied to the circular image. The intensity of each image with varied grayscale values was measured using an optical power and energy meter (PM200, Thorlabs, USA) and measurements are plotted in Fig. 5. The experimental results show that the intensity can be approximately modeled by a linear function of the grayscale value. Based on the experimental data, the light intensity I and the exposure energy E can be modeled as follows:

$$E = It = (0.0021g - 0.061)\, t \quad (3)$$

where g is the grayscale value, E is the exposure energy, I is the intensity, and t is the exposure time. It indicates that the exposure energy can be locally controlled with the grayscale value of the corresponding pixel in the GLVP-SL process.

4.2. Curing characteristics of the resin in GLVP-SL

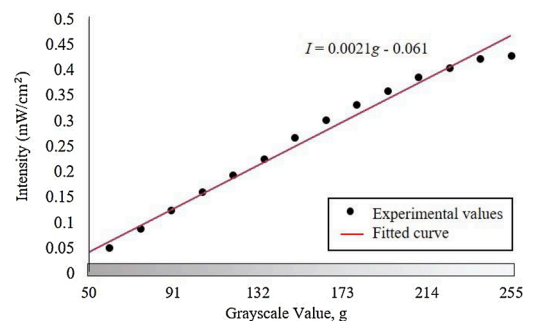To design the grayscale distribution for each mask image, the resin

Fig. 4. Flowchart for the fabrication procedure in the GLVP-SL process.

Fig. 5. Intensity measurement with changing grayscale values.

optical properties, including critical energy threshold (E_c) for initiating the photopolymerization and the penetration depth (D_p) were experimentally determined. The dependence of curing depth as a function of exposure energy is described by the Beer-Lambert law as follows:

$$C_d = D_p * \ln\left(E' / E_c\right) \tag{4}$$

where C_d is the curing depth, and E' is the exposure energy required for target curing depth.

In the GLVP-SL process, if the exposure energy received by a unit liquid is smaller than E' when it reaches its target curing location, it behaves like a liquid or gel and flows past its target curing position, which would lead to distorted printing geometries. However, if the exposure energy a unit liquid received reached to E' before it arrives at its target curing position, a unit liquid gets polymerized before it reaches its target curing position, which would lead to voids in the printed parts. Such insufficient or excessive exposure energy can result in undesirable printing defects [25,26]. The curing depth experiment was conducted to determine the relationship between C_d and E'. A bridge-shaped structure was fabricated using Makerjuice Standard photoresist, as shown in Fig. 6a. Exposure energy of the top layer was controlled by using a set of mask images with different grayscale values and a fixed exposure time of 3 s. These grayscale values were converted to energy using Eq. (3).

The cured thickness of the top layer was then measured using the microscope. The recorded values of exposure energy E' and its resulted curing depths are shown in Fig. 6a. The critical energy threshold E_c for the given resin is around 0.5414 mJ/cm². For a mask image with $E' < E_c$, the resin was not cured. Fig. 6b shows the relationship between C_d and E'. The square dots in the center of each error bar represent the average value of the measured cured depths, while the solid line segment is the one standard deviation of the measured data (3 replicates). The red line is a fitted curve approximated by the following equation:

$$C_d = \begin{cases} 0.0832\ln(E') + 0.1432 \, , \; E \geq E_c \\ 0 \, , \; E < E_c \end{cases} \tag{5}$$

4.3. Modeling of liquid filling in GLVP-SL

In layer-by-layer printing processes based on bottom-up projection, the platform moves up along Z direction to separate the newly cured layer from the resin vat bottom surface. Once separation started, the liquid resin quickly flows into the gap between the newly cured layer and the resin vat bottom surface. The liquid resin filling speed is a function of pressure gradient, the gap distance, the resin viscosity, and the part geometry [27,28]. The pressure gradient and the liquid filling gap distance are determined by the platform moving speed and layer thickness.

In the VP-SL process where the liquid resin keeps flowing towards the light projection area and meanwhile polymerizing, the balance between resin flow speed and polymerizing speed, which was not accounted for under static conditions in the conventional layer-by-layer vat photopolymerization AM processes, is critical to the continuous printing result in VP-SL. The continuous upward movement of the platform applies a continuous suction force on the liquid resin, enabling liquid surrounding the printing region continuously flowing into the projection area and get solidified. To prevent the newly cured material adhere to the resin vat bottom surface and allow for continuous printing, in VP-SL processes, a layer of liquid resin above the resin vat bottom surface needs to maintain in liquid phase, known as a dead zone [10,11,13,14]. Such a dead zone is generated by supplying oxygen to inhibit photo-polymerization. Ideally, to keep this liquid layer from polymerization and maintain it during the continuous printing process, a balance is achieved between the oxygen consumption by continuous photo-polymerization and the oxygen supply from the environment and the bottom oxygen permeable substrate. With the existence of such a constant oxygen-inhibited liquid layer, the pressure gradient in the projection area can be considered as a constant depending on the geometry only, regardless of the platform moving speed or the layer thickness used only for slicing. It implies that the platform moving speed (i.e., printing speed in VP-SL) and slicing layer thickness have negligible effect on liquid flow velocity on the x–y plane.

Using a simplified exponential function to describe the viscosity profile of the liquid during polymerization process, the flow speed of a unit liquid can be modeled as [13]:

$$V_r = \frac{\Delta p}{2\mu e^k r}\left[\left(\frac{h}{2}\right)^2 - \left(z - \frac{h}{2}\right)^2\right] \tag{6}$$

where Δp is the pressure gradient, μ is the liquid viscosity, r is the distance from the liquid unit location to the geometry center of the previous layer, h is the gap distance, z is the Z-axis coordinate of the liquid unit with the resin vat bottom surface being Z = 0, and k is a constant for a certain degree of polymerization. If the liquid does not absorb light energy, k is zero; otherwise, it is a nonzero constant. Consequently, the unit liquid flow speed V_r will further decrease along with the increase of the viscosity due to the continuous photo-polymerization. In our GLVP-SL process, the polymerization degree and the corresponding viscosity coefficient k are controlled by manipulating the g_{min} in the grayscale image design. r depends on the printing geometry size. The oxygen inhibited layer thickness (i.e., the gap distance h) is a combined result of the oxygen consumption and the oxygen supply process, and hence is also dependent on the projection light intensity (which is a function of g_{min} in our approach) and projection area (i.e., layer geometry). It is impossible to characterize the polymerization degree of each unit liquid in situ during a continuous printing process. Although physics-based model Eq. (6) provides a fundamental understanding of the liquid filling speed, it cannot be directly used.

To address this challenge, we developed a statistical model by measuring the flow of a boundary unit liquid (e.g., unit liquid 1
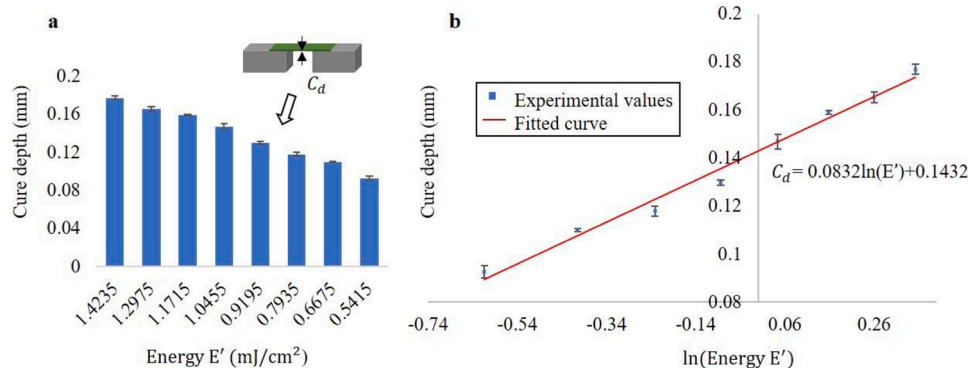

Fig. 6. Relationship between the cure depth and exposure energy: (a) experimental values, (b) relationship curve between C_d and $\ln(E')$.

illustrated in Fig. 2b) during continuous printing. For a proof-of-concept study, we fixed the printing geometry size at 10 mm and fixed the material in our statistical study. As a result, all test cases in this study are geometries that have the longest diameter of 10 mm.

To develop the statistical model of liquid filling, a particle tracking experiment was performed. Aluminum particles (Alpha Chemicals, USA) with a diameter of 30 μm were used as tracers. After mixing resin and particles with a weight ratio of 100:1, the sample was loaded into the resin vat. A set of three different mask images (10 mm x 10 mm) were designed with the grayscale distribution pattern as defined in Eq. (1). Fig. 7a shows the schematic of the experimental setup. A high-speed CCD camera (Pixelink, USA) was integrated with the GLVP-SL setup for motion capture. Images were captured with a selected time interval Δt (0.1 s in this study). The properties of materials along with experimental conditions are presented in Table 1.

Fig. 7b shows optical images of particle movement at four different times during a single layer projection with $g_{min} = 205$. The particle which is used for motion tracking is circled with red color. After obtaining particle positions through image analysis, particle trajectories were reconstructed, and the dimensionless position was measured as the ratio of the maximum distance traveled by particles before solidifying ($R_\varphi - r$ as illustrated in Fig. 2c) and the maximum radius of the mask image (R_φ as illustrated in Fig. 2c). Fig. 7c shows the measured values of δ for three g_{min} values at t = 1.2 s when the projection ends. It was observed that when the g_{min} value was too low (e.g., 190), the particle passed away from its target solidified position (i.e., $\delta = 1.046 > 1$); however, when the g_{min} was too high (e.g., 255), the particle stopped moving and got solidified at $\delta = 0.806$, before arriving at its target position. In contrast, the particle got solidified at its target position (i.e., $\delta = 1$) when the g_{min} value was set at 205.

In order to predict the dimensionless position δ at time t when exposed to the mask images designed with varied g_{min} values, the experimental data was fitted and the dimensionless position δ is modeled as in Eq. (7):

$$\delta = 0.198 + 0.00316\,g_{min} + 0.406\,t - 0.00546\,g_{min}\,t \qquad (7)$$

Table 1
Particle tracking experiment conditions.

Parameter	Value
Printing speed	0.1 mm/s
Gray level	$g_{max} = 255$, $g_{min} = 0$ to 255
Resin density	1.05 g/mL
Resin viscosity	250 cp @ 20 °C
Particle density	1.3 g/cm^3
Particle size	30 μm

4.4. Problem formulation and optimization procedure

As discussed in section 3.1 and illustrated in Figs. 2 and 3, the proposed grayscale distribution for a single layer varies along the radial direction as well as over the time. Considering a mask image with radius R_φ and exposure time T, each sliced image has a unique grayscale distribution with grayscale values from g_{min} to 255, which can be denoted as $g(\delta,t)$. Here, δ is the dimensionless position of a unit liquid at time t. To maintain a successful printing and for a unit liquid to solidify at its target curing position δ_t, it is required that the total exposure energy E should be greater than or equal to the target energy E' (related to the target curing depth). In order to maintain a good bonding between cured polymer, we considered the target curing depth as 1.2 times the layer thickness L [29]. Suppose that at time t_n, a unit liquid moves in the projection area by distance δ_n, gets exposed to mask images with grayscale value g_n and energy E_n. Herein, we present an iterative optimization method for identifying the appropriate g_{min} value at which a unit liquid gets exposed to sufficient energy at its target curing position. Our objective is to minimize the error between total exposure energy E and the target energy E'.

Fig. 8 shows the flowchart to plan the grayscale distribution for mask images based on a minimization objective. The orange box corresponds to the energy iteration, and the blue box corresponds to the grayscale iteration for a single layer. In the first part, we compute the total energy accumulated at position δ, for the initial g_{min} value. In the second part, by comparing E to E', we determine if the resin around position δ will be solidified or not. Based on this comparison, the g_{min} value will be
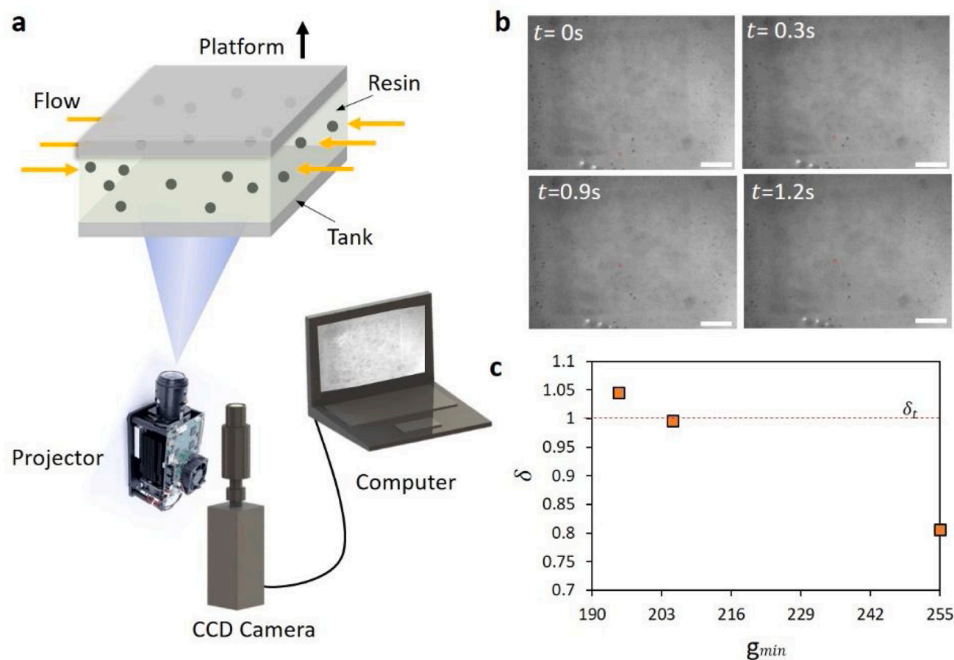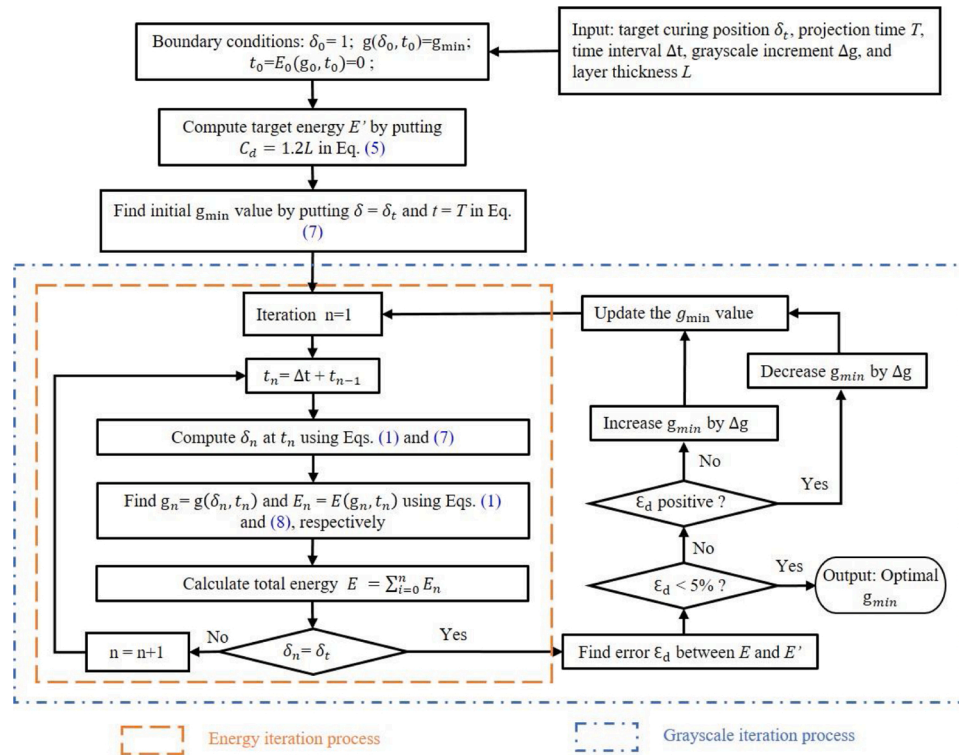

Fig. 7. Particle tracking experiment: (a) experimental setup, (b) optical images at different times after the light projection with $g_{min} = 205$, and (c) recorded δ values for projection with varied g_{min}. The scale bar is 2 mm.

Fig. 8. Flowchart of the optimization process.

increased or decreased. The optimization procedure will stop once the error ε_d between accumulated and target energies is within 5%.

The optimization process begins with defining the target curing position δ_t, projection time T, target energy E', time interval Δt, grayscale increment Δg, and boundary conditions. We assume that to achieve void-free printing, when a unit liquid reaches the center of the layer at time T, its position should be at the center of the mask image 3. Therefore, first, the initial guess for g_{min} value is calculated by putting the values of δ_t and T in Eq. (7). Next, in the first iteration, the δ_1 position of a unit liquid at time t_1 is calculated by substituting Eq. (1) into Eq. (7). It should be noted that the mask image equation is selected based on the time t_1. The respective grayscale value $g(\delta_1, t_1)$ exposed by a unit liquid during GLVP projection at position δ_1 and time t_1 is calculated using Eq. (1). The grayscale value is then used in computing the energy exposed by a unit liquid from time t_0 to t_1 using Eq. (8).

$$E(g,t) = (0.0021g - 0.061)(t_n - t_{n-1}) \tag{8}$$

The process goes on iteratively until δ_n value is equal to δ_t. Finally, the total energy E is calculated by using the sum of all the energies exposed by a unit liquid before reaching its target curing position δ_t, as follows:

$$E = \sum_{i=0}^{n} E(g_n, t_n) \tag{9}$$

The target energy E' is calculated using Eq. (5) which is dependent on the target curing depth. If the difference between the E and E' is greater than the threshold (e.g., 5% used in this test case), then the value of g_{min} will be updated accordingly. For instance, if $E > 1.05 E'$, then we reduce the g_{min} value by Δg; and if $E < 0.95 E'$, increase the g_{min} value by Δg. The process goes on iteratively until the difference is lesser than a threshold error defined by the user, e.g., 5% used in the test cases in this study. Once the g_{min} value satisfies the objective function, mask images are generated using the proposed grayscale distribution design.

5. Result and discussion

To validate the feasibility and effectiveness of the proposed GLVP-SL process for manufacturing solid geometries with a mesoscale cross-section area, three solid geometries with the same largest diameter size 10 mm but different shapes, including cube, pyramid, and cylinder, were printed. Each geometry has been repeatedly printed 3 times as replicates to validate the repeatability and to draw valid conclusions of the proposed approach. The printing speed, projection time for one sliced layer, and mask layer thickness were set at 0.1 mm/s, 1.2 s, and 0.028 mm, respectively. Based on Eq. (5), this geometry requires critical exposure energy of 0.5949 mJ/cm^2 to maintain a successful printing. To demonstrate the versatility of the optimization algorithm, δ_t, Δg and Δt were set as 1, 1, 0.1 s, respectively. According to the flowchart in Fig. 8, for g = 207, we get $E = 0.6004$ mJ/cm^2, which is in the 5% range of the target energy value. Therefore, 207 is considered as the optimum g_{min} value for the model specification. The percentage error for different grayscale values is summarized in Table 2.

After identifying the optimal g_{min} value as 207, the mask images were generated based on the proposed grayscale distributions, and a high frame video was developed for printing the geometry using the GLVP-SL process. For comparison, the same model was printed using the conventional VP-SL process, with the printing speed, projection time, and sliced layer thickness fixed. Optical and microscopic images of the models printed using VL-SL and GLVP-SL processes, respectively, are shown in Fig. 9a–f. From the microscopic images, undesired pores can be observed on the surface of the parts printed using VP-SL. However, no

Table 2
Error calculation for energy consumed by a unit liquid at different g_{min} values.

	g_{min} = 195	g_{min} = 202	g_{min} = 207 (optimum)
E (mJ/cm^2)	0.4986	0.5436	0.6004
E' (mJ/cm^2)	0.5949	0.5949	0.5949
Error (%)	16.1876	8.6233	0.9245

pores were detected on the surface of the parts printed using GLVP-SL.

In addition to comparing the printed surfaces, we also observed the interior microstructure by cutting the printed parts into half. Top views and section views of the cut half of the objects printed using VP-SL and GLVP-SL processes are shown in Fig. 9g and h, respectively. From the top view, it can be observed that the part printed with GLVP-SL has sharper corners than the part printed by the conventional VP-SL process. From the cut cross-section view, it can be observed that the part printed with GLVP-SL has no voids inside the part while the part printed by VP-SL was very porous inside. It should be noted that the rough surface shown in the cross-section view in Fig. 9h is the cut surface. The porosities of the parts printed by GLVP-SL and VP-SL were measured to be 0.04 and 0.15, respectively. A 75 % increase in density was achieved by applying the grayscale mask image video projection approach.

To further validate the effectiveness of the proposed method, we measured the surface roughness of the printed parts using the Nano Contour GT-K Optical Profilometer (Bruker, USA). Fig. 10a–d show the optical image, microscopic image and color map of the roughness distribution on the side surface of the printed parts. Roughness distribution along the X-axis for both parts was compared in Fig. 10e. The roughness value ranging from -5 to 15 µm was observed for the part printed with VP-SL whereas, this value has been significantly reduced down to the range of -2 to 2 µm for the part printed with GLVP-SL. This is 80 % reduction in surface roughness. The undesired voids and rough surface was mainly caused by uncontrolled exposure energy during VP-SL printing. The experimental results validated that these defects can be eliminated in GLVP-SL printing by exposing the liquid resin with controlled energy using the optimum grayscale distribution customized for each video frame. We can conclude that continuous printings of solid objects with improved surface quality could be achieved by the novel GLVP-SL process developed in this study.

6. Conclusion

This paper investigated a novel Gradient Light Video Projection-based Stereolithography (GLVP-SL) method for the continuous production of solid objects. In this method, for each layer, instead of a single binary image, three mask images were designed with unique grayscale distribution patterns. The effect of grayscale values on exposure energy, curing depth, and resin flow were studied. In addition, an optimization model was developed to identify the optimal grayscale parameter setting for designing the grayscale mask images to print a void-free layer with accurate shape. The principle of how spatial and temporal variation of grayscale distribution benefits a unit liquid to solidify at its target curing position was analyzed and experimentally validated. Various solid objects, including cube, pyramid, and cylinder, were printed using the conventional VP-SL and the novel GLVP-SL process. Compared with the conventional VP-SL method, a significantly lower porosity (75% lower) as well as a significantly smaller surface roughness (~80% lower) were achieved by the GLVP-SL process. Experimental results validated the efficiency and effectiveness of the novel GLVP-SL method on the continuous printing of solid objects with accurate geometry and free of voids.

Future work will focus on advancing the application of the developed GLVP-SL process by developing a physics-based machine learning model for the dimensionless position that include more parameters such as the printing geometry size and the resin viscosity.
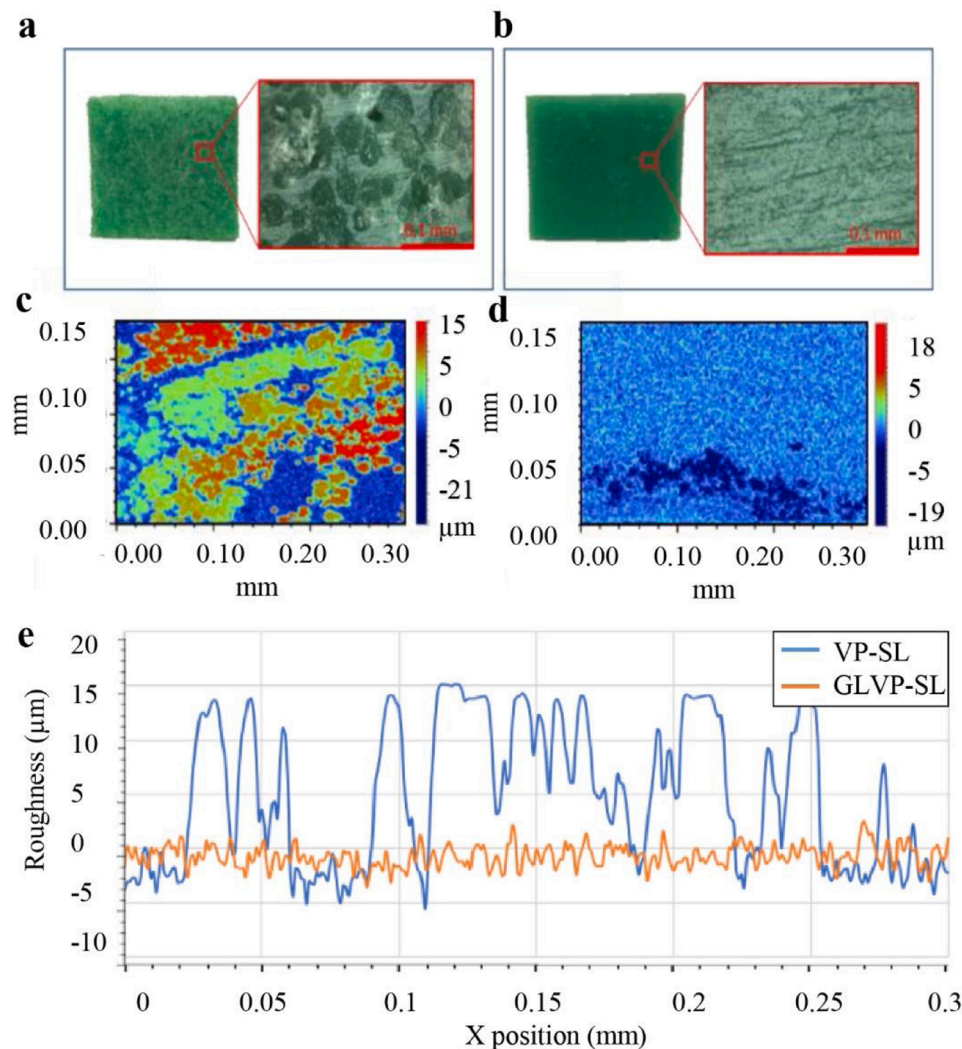
Declaration of Competing Interest

The authors report no declarations of interest.
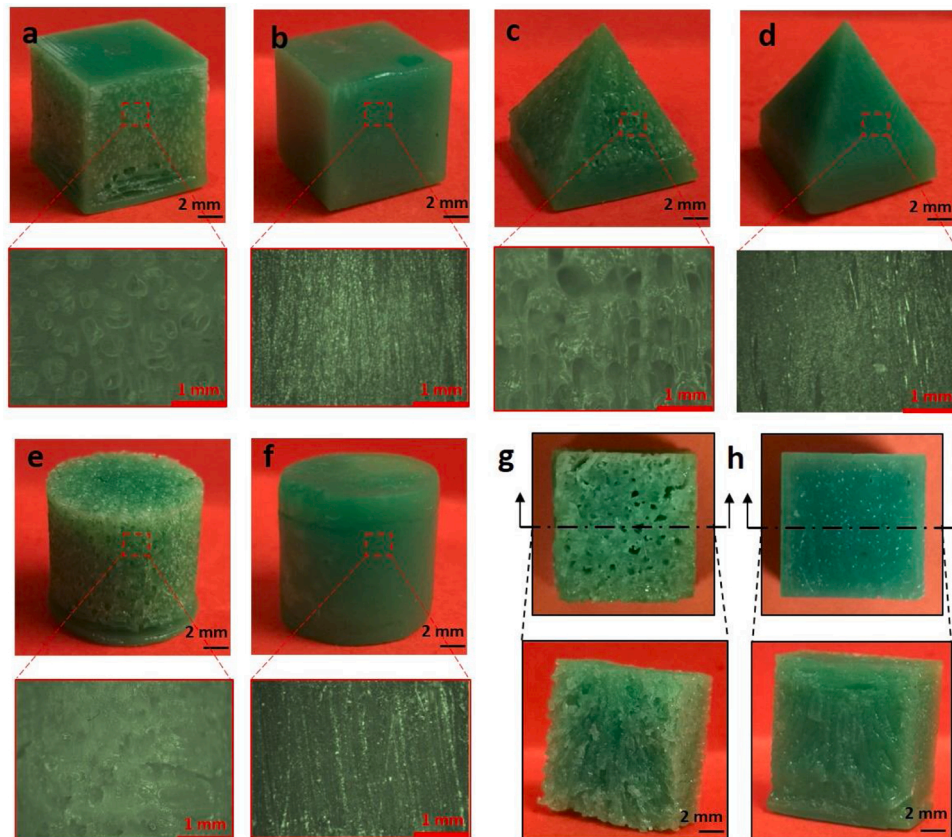
Fig. 9. Photos and microscopic images of geometries printed by VP-SL and GLVP-SL process: (a)-(b) cube, (c)-(d) pyramid, (e)-(f) cylinder; Top view of the printed parts (top row) and cross section view of the parts after cut: (g) part printed by VP-SL, and (h) part printed by GLVP-SL process.

Fig. 10. Roughness characterization: (a) photo and microscopic image of the side surface of the cube model printed by the conventional VP-SL process, (b) photo and microscopic image of the side surface of the cube model printed by our GLVP-SL process, (c) the color map of surface roughness of the side surface shown in (a), (d) the color map of surface roughness of the side surface shown in (b), and (e) comparison of surface roughness measurements of the two surfaces shown in (a) and (b).

Acknowledgments

References

[1] Zhou C, Chen Y. Calibrating large-area mask projection stereolithography for its accuracy and resolution improvements. 20th Annu. Int. Solid Free. Fabr. Symp. SFF 2009 2009:82–97.

[2] Cheng YL, Lee ML. Development of dynamic masking rapid prototyping system for application in tissue engineering. Rapid Prototyp J 2009;15:29–41. https://doi.org/10.1108/13552540910925045.

[3] Choi JW, Wicker R, Lee SH, Choi KH, Ha CS, Chung I. Fabrication of 3D biocompatible/biodegradable micro-scaffolds using dynamic mask projection microstereolithography. J Mater Process Technol 2009;209:5494–503. https://doi.org/10.1016/j.jmatprotec.2009.05.004.

[4] Melchels FPW, Feijen J, Grijpma DW. A review on stereolithography and its applications in biomedical engineering. Biomaterials 2010;31:6121–30. https://doi.org/10.1016/j.biomaterials.2010.04.050.

[5] Yang Y, Chen Z, Song X, Zhang Z, Zhang J, Shung KK, et al. Biomimetic anisotropic reinforcement architectures by electrically assisted nanocomposite 3D printing. Adv Mater 2017;29. https://doi.org/10.1002/adma.201605750.

[6] Kruth JP. Material Incress Manufacturing by Rapid Prototyping Techniques. CIRP Ann Manuf Technol 1991;40:603–14. https://doi.org/10.1016/S0007-8506(07)61136-6.

[7] Matthey J, Ian Gibson B, Edgar J, Tint S. "Additive Manufacturing Technologies: 3D Printing, Rapid Prototyping, and Direct Digital Manufacturing", 2nd Edition. Technol Rev 2015:193–8. https://doi.org/10.1595/205651315X688406.

[8] Stansbury JW, Idacavage MJ. 3D printing with polymers: challenges among expanding options and opportunities. Dent Mater 2016;32:54–64. https://doi.org/10.1016/j.dental.2015.09.018.

[9] Januszewicz R, Tumbleston JR, Quintanilla AL, Mecham SJ, DeSimone JM. Layerless fabrication with continuous liquid interface production. Proc Natl Acad Sci U S A 2016;113:11703–8. https://doi.org/10.1073/pnas.1605271113.

[10] He H, Yang Y, Pan Y. Machine learning for continuous liquid interface production: printing speed modelling. Int J Ind Manuf Syst Eng 2019;50:236–46. https://doi.org/10.1016/j.jmsy.2019.01.004.

[11] Tumbleston JR, Shirvanyants D, Ermoshkin N, Januszewicz R, Johnson AR, Kelly D, et al. Continuous liquid interface production of 3D objects. Science 2015;347(80-):1349–52. https://doi.org/10.1126/science.aaa2397.

[12] Pan Y, Zhou C, Chen Y, Partanen J. Multitool and multi-axis computer numerically controlled accumulation for fabricating conformal features on curved surfaces. J Manuf Sci Eng Trans ASME 2014;136. https://doi.org/10.1115/1.4026898.

[13] Jiang Y, Wang Y, He H, Feinerman A, Pan Y. Constrained Window Design in Projection Stereolithography for Continuous Three-Dimensional Printing. 3D Print Addit Manuf 2020;7:163–9. https://doi.org/10.1089/3dp.2019.0134.

[14] Jiang Y, Wang Y, Lichade K, He H, Feinerman A, Pan Y. Textured window design for continuous projection stereolithography process. Manuf Lett 2020;24:87–91. https://doi.org/10.1016/j.mfglet.2020.04.007.

[15] Li X, Mao H, Pan Y, Chen Y. Mask Video Projection-Based Stereolithography with Continuous Resin Flow. J Manuf Sci Eng Trans ASME 2019;141:1–10. https://doi.org/10.1115/1.4043765.

[16] Walker DA, Hedrick JL, Mirkin CA. Rapid, large-volume, thermally controlled 3D printing using a mobile liquid interface. Science 2019;366(80-):360–4. https://doi.org/10.1126/science.aax1562.

[17] Ma X, Kato Y, Kempen F, Hirai Y, Tsuchiya T, Keulen F, et al. Multiple patterning with process optimization method for maskless DMD-based grayscale lithography. Procedia Eng 2015;120:1091–4. https://doi.org/10.1016/j.proeng.2015.08.778.

[18] Zhou C, Chen Y. Additive manufacturing based on optimized mask video projection for improved accuracy and resolution. J Manuf Process 2012;14:107–18. https://doi.org/10.1016/j.jmapro.2011.10.002.

[19] Zhou C, Chen Y, Waltz RA. Optimized mask image projection for solid freeform fabrication. J Manuf Sci Eng Trans ASME 2009;131:0610041–06100412. https://doi.org/10.1115/1.4000416.

[20] Park IB, Ha YM, Lee SH. Dithering method for improving the surface quality of a microstructure in projection microstereolithography. Int J Adv Manuf Technol 2011;52:545–53. https://doi.org/10.1007/s00170-010-2748-6.

[21] Guangshen X, Songqiao H, Huan P, Jing J, Sheng L, Ronghua Q. Research of a novel integral stereolithography system for microstructures. 2009 2nd Int. Conf. Intell. Comput. Technol. Autom. ICICTA 2009, 2; 2009. p. 880–3. https://doi.org/10.1109/ICICTA.2009.448.

[22] Bonada J, Muguruza A, Fernández-Francos X, Ramis X. Optimisation procedure for additive manufacturing processes based on mask image projection to improve Z accuracy and resolution. J Manuf Process 2018;31:689–702. https://doi.org/10.1016/j.jmapro.2018.01.004.

[23] Pan Y, Chen Y. Smooth surface fabrication based on controlled meniscus and cure depth in microstereolithography. J Micro Nano-Manufacturing 2015:3. https://doi.org/10.1115/1.4030661.

[24] Wang Y, Xue D, Mei D. Projection-based continuous 3D printing process with the grayscale display method. J Manuf Sci Eng 2020:142. https://doi.org/10.1115/1.4045616.

[25] Emami MM, Barazandeh F, Yaghmaie F. Scanning-projection based stereolithography: Method and structure. Sens Actuators A Phys 2014;218:116–24. https://doi.org/10.1016/j.sna.2014.08.002.

[26] Fang N, Sun C, Zhang X. Diffusion-limited photopolymerization in scanning micro-stereolithography. Appl Phys A Mater Sci Process 2004;79:1839–42. https://doi.org/10.1007/s00339-004-2938-x.

[27] Gritsenko D, Ahmadian Yazdi A, Lin Y, Hovorka V, et al. On characterization of separation force for resin replenishment enhancement in 3D printing. Addit Manuf 2017;17:151–6. https://doi.org/10.1016/j.addma.2017.08.010.

[28] Pan Y, He H, Xu J, Feinerman A. Study of separation force in constrained surface projection stereolithography. Rapid Prototyp J 2017;23:353–61. https://doi.org/10.1108/RPJ-12-2015-0188.

[29] Gojzewski H, Guo Z, Grzelachowska W, Ridwan MG, Hempenius MA, Grijpma DW, et al. Layer-by-Layer Printing of Photopolymers in 3D: How Weak is the Interface? ACS Appl Mater Interfaces 2020;12:8908–14. https://doi.org/10.1021/acsami.9b22272.